Electrical Properties of Tin Dioxide Two-Dimensional Nanostructures

Elisabetta Comini,*,† Vincenzo Guidi,‡ Cesare Malagù,‡ Giuliano Martinelli,‡ Z. Pan,§ Giorgio Sberveglieri,† and Zhong L. Wang§

INFM and Università di Brescia, Via Valotti 9, 25133 Brescia, Italy, INFM, INFN Sezione di Ferrara, Università di Ferrara, Via Paradiso, 44100 Ferrara, Italy, and Center for Nanoscience and Nanotechnology, School of Materials Science and Engineering, Georgia Institute of Technology, Atlanta, Georgia 30332-0245

Received: September 9, 2003; In Final Form: November 26, 2003

Tin dioxide is the most used material for gas sensing because its three-dimensional nanostructures and properties are related to the large surface exposed to gas adsorption. We propose the use of a two-dimensional nanostructure of SnO_2 in the form of nanobelts; such newly achieved layers have been found to exhibit electrical properties that are similar to their three-dimensional counterpart but with the unique feature of being a pure crystal. Such a characteristic would guarantee long-term stability for the nanobelts, a condition which is not always met with three-dimensional nanostructures because of the occurrence of grain coalescence. In this framework, we developed an analytical approach to model the electrical properties of one-, two-, or three-dimensional nanostructures.

1. Introduction

Solids with a grain size of a few nanometers are normally referred to as nanocrystalline materials: they exhibit properties that are significantly different from their coarse-grained polycrystalline counterparts. A first classification of the change to the properties of a material relies on either "bulk" or "surface" effects. Typically bulk effects involve the confinement of electrons in nanometric cells, which cause quantum phenomena to take place; an emblematic example is the dramatic change of optical properties of nanostructured silicon.[1] Surface effects normally appear because of the magnification in the specific surface of nanostructures, leading to the enhancement of the properties related to that, such as catalytic activity or surface adsorption.

This latter is the basic phenomenon underlying a class of devices, i.e., solid-state gas sensors, which have rapidly emerged because of the immense field of applications they can be used in. In the past decade, a big effort was made in the search for novel materials.[2] Among these, particular focus was given to mixed-oxide semiconductors, which are capable of sensing parts per million or even parts per billion concentration of a gaseous species through the modulation of the intergrain energy barrier in a polycrystalline film.[3] Here the extension of the specific surface exposed to gas adsorption leads to sensitivity improvement of the layer as a sensor. The advent of reproducible and relatively simple methodologies for preparation of nanostructured layers has led the research still further. In this regard there are many articles in the literature about nanostructured films featuring superior performance with respect to their coarse-grained polycrystalline counterparts.

Nanocrystalline materials are classified into different categories depending on the number of dimensions which are nanostructured: the generally acknowledged classification is[2] layered nanostructures (one nanostructured dimension, 1D), filamentary structures (2D), and equiaxial nanostructured materials (3D). The realization and the study of 1D and 3D nanostructures were actively explored,[4] whereas the 2D structures have been less investigated.

For gas sensing, typically a three-dimensional (3D) nanostructure is considered. However, 3D nanostructures often highlight a tendency to change the electrical properties owing to grain coalescence, porosity modification, and grain-boundary alteration. The problem becomes still more complex because the layers must be kept at a relatively high temperature in order to guarantee the reversibility of chemical reactions at the surface. Thus, several solutions have been put forward to stabilize the nanostructure, e.g., addition of a foreign element[5] or phase.[6] A technique that renders the material sufficiently crystalline to guarantee long-term stability while maintaining a high sensitivity would be the optimal. As pointed out in ref 7, a 2D structure such as a nanobelt could potentially fulfill both requirements.

In this paper we aim at investigating the structural and electrical features of 2D nanostructures and demonstrate that such systems can be profitably used as candidate materials for gas sensing. We focused on SnO_2 because that is the most studied and used material for gas sensing through solid-state devices.

2. Experimental Section

The experimental setup used for the synthesis of SnO_2 consists of a horizontal cylindrical furnace, an alumina tube, a rotary pump system, and an atmosphere supply and control system.[8] Commercial (Alfa Aesor) SnO or SnO_2 powder with a purity of 99.9% (metals basis) was used as the source material that was placed in an alumina crucible; this latter was located at the center of the alumina tube. Several alumina strip plates (60×10 mm^2) were placed downstream one by one inside the alumina tube, which acted as substrates for collecting growth products. After evacuation of the alumina tube to $\sim 2 \times 10^{-3}$ Torr, thermal evaporation was conducted at 1000 °C for SnO powder or 1350 °C for SnO_2 powder for 2 h under 300 Torr of Ar gas at a flow rate of 50 sccm. The process of material growth inside the alumina tube was monitored in situ through a quartz window installed at the gas inlet end of the alumina tube during the evaporation. A white wool-like product was collected in a

* Corresponding author. Telephone: +39 030 3715706. Fax. +39 030 2091271. E-mail: comini@tflab.ing.unibs.it.
† Università di Brescia.
‡ Univesità di Ferrara.
§ Georgia Institute of Technology.

10.1021/jp036693y CCC: $27.50
Published on Web 01/14/2004

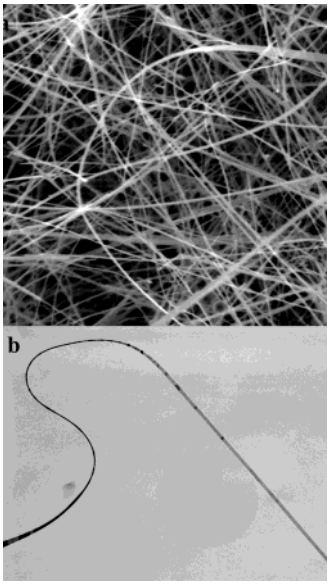

Figure 1. (a) SEM image of SnO_2 nanobelts grown by a solid−vapor process. (b) Single crystal.

narrow region downstream, where the temperature was in the range of 900−950 °C. Similar nanostructures were obtained at the same temperature zone whether the source material was SnO or SnO_2. The as-synthesized material was characterized by X-ray diffraction (XRD) (Philips PW1800 diffractometer with Cu target), scanning electron microscopy (SEM) (Hitachi S800 FEG), transmission electron microscopy (Hitachi HF-2000 FEG at 200 kV and JEOL 4000EX high-resolution TEM at 400 kV), and energy-dispersive X-ray spectrometry (EDS).

To characterize the electric properties of tin oxide nanobelts, depositions were made also onto 3×3 mm^2 alumina substrates. These substrates were provided with interdigitated contacts and heaters deposited by sputtering from a platinum target. The heater is a meander of platinum that acts also as a temperature sensor; it allows operation between room temperature and 600 °C.

We have measured the electrical properties of the nanobelts in a flux of wet synthetic air [0.3 L/min, 30% relative humidity (RH)] and in the presence of an air pollutant such as NO_2 or ethanol. The flow-through technique was used to test the gas-sensing properties of the thin films. A constant flux of synthetic air of 0.3 L/min was the gas carrier. The desired concentrations were obtained from certified bottles and a mixing system with mass flow controllers described in ref 9.

3. Structural Characterization

The as-synthesized material consists of a large amount of ultralong nanobelts (Figure 1a). The morphology depicted in Figure 1a is particularly suitable for gas sensing owing to a large number of interbelt contacts, which allow the percolation of current. Figure 1b shows an individual nanobelt, which well justifies the 2D approach adopted in the modeling (see section 4). Typically, the tin oxide nanobelts are several hundred micrometers in length; some of them even have lengths on the order of millimeters. The chemical composition of the nanobelts was determined to be SnO_{2-x}, where $x = 0-0.2$ with consideration of the margin of error in EDS measurements. Probably this is an indication of the presence of oxygen vacancies causing an n-type doping to the semiconductor similar to the 3D counterpart. This hypothesis on the semiconducting behavior of the layer, which is mandatory for exploitation as a gas sensor, will be investigated later in this work.

XRD analysis indicates that the nanobelts have a rutile-type structure with lattice constants $a = 4.732$ Å and $c = 3.184$ Å, which are consistent with those of bulk SnO_2. Differently from the 3D nanostructures, the nanobelts are structurally perfect and uniform, with 30−200 nm widths, the width-to-thickness ratio being ∼5−10, and lengths of several hundred micrometers to a few millimeters. The nanobelt grows along [101], and it is enclosed by (010)/($0\bar{1}0$) and ($10\bar{1}$)/($\bar{1}01$) crystal facets. On one hand this peculiarity allows a large specific surface exposed for gas sensing, and on the other hand it envisages long-term stability due to the crystallinity of the nanobelts. Further details on the structure of such nanobelts can be found in ref 10.

4. Modeling

Since we are investigating a novel topology of a material for gas sensing, we developed a model that is capable of interpreting and comparing the properties of 1D, 2D, and 3D nanostructures. Such materials exhibit a significant surface-to-volume ratio; thereby a large fraction of the atoms resides at the grain boundary. In particular, for the purpose of this work, we will focus on the shape of the built-in potential that originates when the nanostructure is interfaced with gas.

The built-in potential V_{bi} and the related Schottky barrier height (SBH) that originate at the interface are presently under study, but the interpretation is still unsatisfactory if compared to the widespread technological outcome of nanocrystalline semiconductors, e.g., as rectifying contacts[11,12] and as gas sensors.[13,14] The main aspect which has frustrated attempts at a truly predictive theory is the presence of a high density of surface states, which causes the so-called pinning of the Fermi level.[15] In many cases this effect, which prevents these materials from being used as Schottky devices, owing to the SBH independence of the work function of the metal or of the gas interfaced with the nanostructure, has been technologically solved.[16] A sort of Fermi level "unpinning" has indeed been observed as the dimensions become comparable to the depletion layer depth at the boundaries of the nanocrystals.[17]

The model here proposed takes into account the unpinning of the Fermi level and the different behavior of the nanostructure when they reach dimensions comparable to the depleted region. In the latter case the dimensionality is a crucial parameter as will be shown in the following.

To this aim, the Poisson equation will be solved for the electrostatic potential $\phi(r)$, which is defined as (minus) the band bending at a distance r from the center of the grain. The charge density to be used in the Poisson equation is determined in the literature by fixing the zero value for the electrostatic potential in the conduction band bottom of the bulk.[18,19] Consequently, the depletion approximation (DA), for which the boundary conditions require the existence of a region where the potential and the field are identically zero, is applicable only to those nanostructures where the bulk is attained at least on the center of the nanocrystals. In this case, the equation depends on the dimensionality of the system as follows:

$$\frac{\partial^2\phi(r)}{\partial r^2} = -\frac{eN_d}{\epsilon} \qquad \text{(1D)} \qquad (1.1)$$

$$\frac{\partial^2\phi(r)}{\partial r^2} + \frac{1}{r}\frac{\partial\phi(r)}{\partial r} = -\frac{eN_d}{\epsilon} \qquad \text{(2D)} \qquad (1.2)$$

$$\frac{\partial^2\phi(r)}{\partial r^2} + \frac{2}{r}\frac{\partial\phi(r)}{\partial r} = -\frac{eN_d}{\epsilon} \qquad \text{(3D)} \qquad (1.3)$$

N_d is the density of the ionized donors, which holds in the space charge layer, e.g., for $R_o < r < R$, where R is the radius

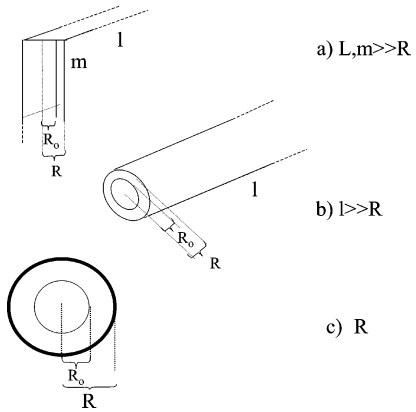

Figure 2. Classification of nanostructures: (a) 1D-layered (lamellar), (b) 2D-cylindrical (filamentary), (c) 3D-spherical (crystallites). The region extending from the central plane (1D), row (2D), or point of the nanocrystal along the distance R_o is the bulk neutral region.

of the nanocrystal and is zero for $r < R_o$ (see Figure 1); e is the electron charge; and ϵ is the permittivity of the semiconductor. The first term of the equations is the Laplacian in rectilinear (1D), cylindrical (2D), and spherical (3D) coordinates, where the angular dependence is not considered because of the assumed symmetry of the single nanocrystals.

In this case the boundary conditions are

$$\phi(r \leq R_o) = 0$$
$$-\left.\frac{\partial \phi}{\partial r}\right|_{r \leq R_o} = 0 \qquad (2)$$

The geometry of the three cases is sketched in Figure 2, where it can be seen that the dimensions of the nanocrystals allow the potential to extinguish in the bulk neutral region, i.e., for $r < R_o$. This leads to the following analytical solutions:

$$\phi(r) = -\frac{eN_d}{2\epsilon}(r - R_o)^2 \qquad \text{(1D)} \qquad (3.1)$$

$$\phi(r) = -\frac{eN_d}{4\epsilon}\left[(r^2 - R_o{}^2) - 2R_o{}^2 \log\frac{r}{R_o}\right] \qquad \text{(2D)} \qquad (3.2)$$

$$\phi(r) = -\frac{eN_d}{6\epsilon}\left(r^2 - 3R_o{}^2 + 2\frac{R_o{}^3}{r}\right) \qquad \text{(3D)} \qquad (3.3)$$

As a practical example, we calculate such solutions for the experimental values obtained in the literature: the built-in potential derived from electrical measurements[20] is $V_{bi} = -\phi(r{=}R) = 0.68$ V; substituting this condition in eqs 3, we found the values of R_o and, consequently, the depletion region. The values $N_d = 5 \times 10^{18}$ cm^{-3} and $\epsilon = 10^{-10}$ F/m were obtained elsewhere,[21] and the resulting potential shapes for $R = 50$ nm are plotted in Figure 3. Regarding the doping level, it was assumed to be of the same order of magnitude as that for 3D structures owing to the electrical conductance measurements shown in the next section. We plotted the solution of eqs 3 with this value for R because it represents the characteristic dimensional parameter of the nanobelts concerned in this work.

It is interesting to notice that, even if the form of the solution is very different and depends on the dimensionality of the problem (see eqs 5−7), it does not lead to an appreciable difference in the potential extinction length: $R_o = 37$ nm (1D), $R_o = 36.5$ nm (2D), and $R_o = 35.4$ nm (3D). Consequently, no significant change in the sensitivity versus gases is expected

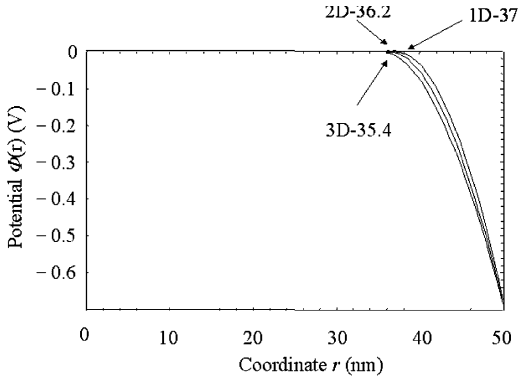

Figure 3. Potential shape versus coordinate r calculated on the basis of eqs 3 with the experimentally determined parameters. Nanocrystal dimensions: $R = 50$ nm for 1D, 2D, 3D.

for the 2D structures with respect to the 3D counterpart, as will be highlighted in next section.

Any differences induced by dimensionality are expected when the nanostructure reaches dimensions comparable to or less than the calculated depletion region, e.g., $R - R_o \approx 15$ nm.

Although the experimental parameters for the nanobelts under study allow the solution expressed above, for the sake of generality, we propose the natural extension of the model to a still lower grain size.

In the literature, the surface density of states is normally referred to as N_t, which represents the amount of chemisorbed surface species per unit area that induce electronic energy levels into the band gap of the semiconductor. It is widely accepted that they are the main cause for the Fermi level pinning for metal oxide semiconductors.[22,23]

Let us now consider the case of a crystal dimensions less than the potential extinction region or depleted region. Here the depletion approximation does not hold and the Poisson equations must be written with the complete charge density:

$$\frac{\partial^2 \phi(r)}{\partial r^2} = -\frac{eN_d}{\epsilon} + \frac{eN_d}{\epsilon}\exp\left[\frac{e\phi(r)}{k_B T}\right] \qquad \text{(1D)} \qquad (4.1)$$

$$\frac{\partial^2 \phi(r)}{\partial r^2} + \frac{1}{r}\frac{\partial \phi(r)}{\partial r} = -\frac{eN_d}{\epsilon} + \frac{eN_d}{\epsilon}\exp\left[\frac{e\phi(r)}{k_B T}\right] \qquad \text{(2D)} \qquad (4.2)$$

$$\frac{\partial^2 \phi(r)}{\partial r^2} + \frac{2}{r}\frac{\partial \phi(r)}{\partial r} = -\frac{eN_d}{\epsilon} + \frac{eN_d}{\epsilon}\exp\left[\frac{e\phi(r)}{k_B T}\right] \qquad \text{(3D)} \qquad (4.3)$$

These equations differ from the corresponding ones in eqs 1 only for the term representing the mobile charge, which depends exponentially on the potential and makes the solutions of these equations nonanalytical. Since the potential is always nonpositive[24] and its value is very near the level at the surface in the whole nanocrystal, because of the short distance between the surface and the center of the grain, we can consider it to be much larger than $k_B T$, where k_B is the Boltzmann constant. Therefore, the second term is negligible. The same equations as eqs 1 are thus obtained, but the physical difference is expressed by the boundary conditions. In this case, in fact, there is no neutral region and therefore R_o can no longer be defined; i.e., the whole crystal is almost depleted of mobile charge. For symmetry reasons it is easy to show that the condition

$$-\left.\frac{\partial \phi}{\partial r}\right|_{r=0} = 0 \qquad (5)$$

still holds.

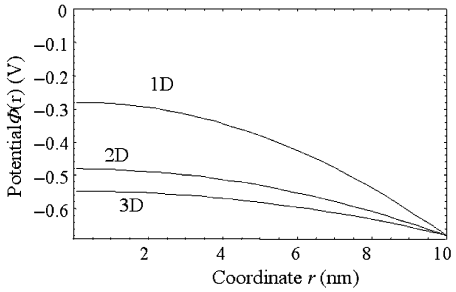

Figure 4. Potential shape versus coordinate r calculated on the basis of eqs 7 with the experimentally determined parameters. Nanocrystal dimensions: $R = 10$ nm, i.e., less than the potential extinction length, for 1D, 2D, 3D.

The condition for the potential is now

$$-\phi|_{r=R} = V_{bi} \tag{6}$$

The solutions of eqs 4 provided with these boundary conditions are

$$\phi(r) = -\frac{eN_d}{2\epsilon}(r^2 - R^2) - V_{bi} \qquad (1D) \qquad (7.1)$$

$$\phi(r) = -\frac{eN_d}{4\epsilon}(r^2 - R^2) - V_{bi} \qquad (2D) \qquad (7.2)$$

$$\phi(r) = -\frac{eN_d}{6\epsilon}(r^2 - R^2) - V_{bi} \qquad (3D) \qquad (7.3)$$

These solutions appear to be formally identical, if not for a numerical factor: this is the opposite situation as the previous case, where the solutions appeared to be qualitatively different but led to very similar values for the potential extinction length. In this case, to plot the three solutions, the value of the surface potential V_{bi} is unessential because it is only an offset. However, we assumed that this value is not very different from the built-in potential measured in our crystals. In fact, the gas−semiconductor interface is the same and thereby the value of surface potential with respect to the bulk is not expected to change for the two cases. In Figure 4 we can see the comparison between the three solutions in the case of $R = 10$ nm, and it is clearly seen that the potential on the center of the grain is near the value at the surface, especially for the 3D case. This effect is the theoretical interpretation[24] for the flattening of the band bending experimentally determined in ref 25. Now the band bending, which is $\phi(0) - \phi(R)$ by definition, is 0.4 V (1D), 0.2 V (2D), and 0.14 V (3D).

It is clear that $\phi(0) - \phi(R)$ depends considerably on the dimensionality of the nanocrystals. Moreover, from the knowledge of the potential shape, it is possible to calculate the surface field and to connect it to the density of chemisorbed surface states via the Gauss theorem:

$$-\left.\frac{\partial\phi}{\partial r}\right|_{r=R} = \frac{eN_t}{\epsilon} \tag{8}$$

This represents the neutrality condition of the single nanocrystals. By substituting eqs 7 in eq 8, it is easily shown that N_t decreases linearly with the grain radius R leading to the unpinning effect as R reaches nanometric dimensions, the strongest effect being obtained for the 3D case.

5. Chemoresistive Electrical Properties

In this section, we aim at highlighting that the electrical properties and sensitivity to gases of nanobelts are equivalent to those of their 3D counterparts, as deduced from the model. Electrical characterization consisted of two parts: first a study about the conductive properties of the films exposed to a flux of humid synthetic air, and then an investigation on the sensing capability of the layers toward NO_2, a gas of great importance for air-quality monitoring in urban areas, and ethanol, for breath analyzers and food quality control.[26]

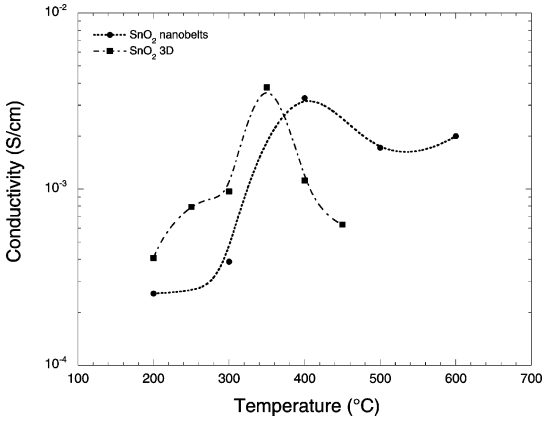

Figure 5. Conductivity of nanobelts and 3D tin dioxide thin films as a function of operating temperature in a flux of synthetic air of 0.3 L/min and 30% RH. The same behavior of conductivity versus temperature can be pointed out. The temperature of the maximum conductivity corresponds to the maximum oxygen chemisorption for the tin oxide layers.

As we modeled in last section, the electrical behavior of the thin films can be interpreted within the framework of the existing theory on chemical sensors. It is known in the literature[27] that the resistance of semiconducting thin films is strongly influenced by the presence of oxidizing or reducing gases. The molecules of gas may interact with the surface of the semiconductor and then be adsorbed on it. There are two major categories for adsorption of a gas on a solid surface: physisorption and chemisorption. In the latter case the bonding is strong and, normally, the molecules dissociate into atoms, while in the former case the bonding is weak and is usually associated with dipole-to-dipole interaction between adsorbate and adsorbent. At low temperatures the rate of chemisorption is so low that equilibrium cannot be reached in real time and thus the chemisorbed volume is low. Surface coverage by chemisorbed species first increases with temperature, until an equilibrium state is reached, and then starts to decrease because of desorption processes. Oxygen in the atmosphere is adsorbed on the surface of the semiconductor as different species (O_2, O_2^-, and O^-). The adsorbate acts as a surface state (with a density N_t) by capturing electrons, which are held to the surface by electrostatic attraction; this mechanism causes the resistance of the films to grow despite a temperature increase.

Following the literature, the response of a sensor is defined as the normalized variation of resistance for an n-type semiconductor and oxidizing gases ($S = \Delta R/R_0$), while for reducing gases it is defined as the normalized variation of conductance for a n-type semiconductor ($S = \Delta G/G_0$). The response (τ_{res}) and recovery (τ_{rec}) times are two parameters qualifying the rapidity of a sensor to vary in resistance when a test gas is present (R_f; G_f) and when it is not (R_0; G_0) and vice versa. These are operatively defined as the times taken to reach 90% of $R_f - R_0$, $G_f - G_0$ when the gas is being introduced and to recover to 30% of $R_f - R_0$, $G_f - G_0$ when the flux of air is being restored.

Figure 5 shows the conductivity of the tin dioxide nanobelt layers and, for comparison, of a polycrystalline (3D) thin film of tin oxide (300 nm thick, grain size about 20 nm) as a function

of the operating temperature in a flux of synthetic air. Regarding nanobelts, we observed a maximum for conductivity at 400 °C corresponding to the maximum value of oxygen coverage. The behavior of 3D films is the same as a function of the working temperature, with a maximum at 350 °C instead of 400 °C. This discrepancy can be explained in terms of a difference between the nominal temperature of the upper side of the substrate and the tin oxide effective temperature in the case of the nanobelts due to nonuniform contact between the substrates and the nanobelt structures. The curves presented follow the typical behavior due to competition between adsorption of oxygen species and capture of electrons.[28] The decrease in resistivity due to temperature increase from room temperature to 400 °C is mainly due to the increase in O_2^- chemisorption, as has already been reported for zinc and tin oxides.[29] At 400 °C for 2D structures and 350 °C for 3D structures, adsorption process reached an equilibrium state with the desorption process and resistivity began to increase.

The semiconductor sensing properties are based on reactions between the semiconductor and the gases in the atmosphere, which cause a change in the semiconductor's resistance due to charge transfer between the adsorbate and the adsorbent. In the case of NO_2, there are proofs of reactions directly with the semiconductor surface other than with the oxygen chemisorbed at the surface. Tamaki et al.[30] studied nitrogen dioxide absorption on tin oxide surfaces by temperature programmed desorption measurements and found that the adsorbates originating from NO_2 are essentially the same as those for NO, since NO_2 molecules dissociate easily over the tin oxide surface. These adsorbates can be divided into three different types: two nitrosyl types, Sn−NO^+ and Sn−NO^-; and the nitrite type, Sn−O−N═O. The nitrite type does not play a role in gas sensing since it is not involved in any electron exchange with the bulk of the semiconductor. These results are in agreement with the work of Solymosi and Kiss,[31] who proposed the following reactions:

$$NO_g + e \rightarrow NO^-_{chem}$$

$$NO_g \rightarrow NO^+_{chem} + e$$

Where the second type of absorption is much weaker than the first one, Ghiotti et al.[32] proposed similar reactions based on Fourier transform infrared spectroscopy measurements. The shape of the kinetic response can be explained by an increase in the height of the surface barriers at grain interfaces due to electron trapping in NO chemisorbed molecules. Figure 6 shows the variation of the conductance as 500 ppb nitrogen dioxide was fed into the test chamber; the conductance of the layer decreased rapidly and, when the air flux was restored, it returned to the stable value. The response time toward nitrogen dioxide is very short, less than 30 s, whereas the recovery time is high, more than 10 min. This problem is, however, well-known for this kind of gas.[33] Figure 7 shows the response toward 500 ppb nitrogen dioxide as a function of the operating temperature. The highest value of the response is more than 15 at 300 °C. The maximum of the response is obtained for relatively low temperatures, due to the particular reaction mechanism of NO_2 with SnO_2. The sensor response, compared to the one found in the literature for a thin film of sputtered tin oxide toward nitrogen dioxide, is about 1 order of magnitude higher (1.3 toward 500 ppb[34]). This behavior can be explained by the enormously higher surface-to-volume ratio of the nanobelts with respect to the polycrystalline morphology that increases the number of possible reaction sites.

The mechanism of ethanol sensing is complex and not yet completely established. A scheme for interpretation of the

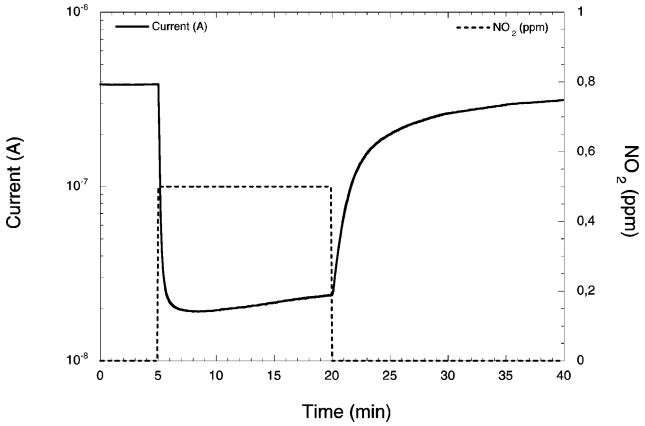

Figure 6. Variation of current flowing through the nanobelts at a working temperature of 300 °C and 30% RH, as 500 ppb nitrogen dioxide is introduced in the test chamber. The conductance of the layer decreases rapidly, and when the air flux is restored, it returns to the stable value. The response time toward nitrogen dioxide is very short, less than 30 s, whereas the recovery time is high, more than 10 min.

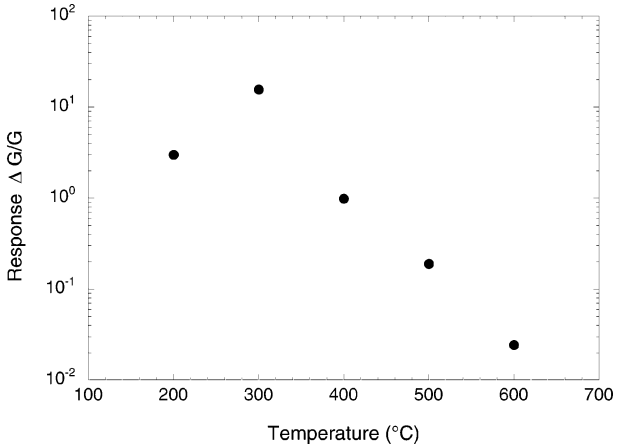

Figure 7. Response of tin oxide nanobelts toward 500 ppb NO_2 as a function of operating temperature at 30% RH. The highest value of the response is more than 15 at 300 °C. The maximum of the response is obtained for relatively low temperatures, due to the particular reaction mechanism of NO_2 with SnO_2.

transformation of ethanol to aldehyde[26] through catalytic interaction with a MOS surface has recently been proposed. The dissociation of ethanol produces an ionic bond between the oxygen in the molecule and unsaturated metal site, while the hydrogen atom is bound to a nearby oxygen anion:

$$CH_3CH_2OH + O(s) + M(s) \rightarrow CH_3CH_2O{-}M(ads) + O{-}H(ads) \rightarrow CH_3CHO + H{-}M(ads) + O{-}H(ads)$$

where (s) and (ads) indicate a surface site and an adsorbed species, respectively.

The residual hydrogen from ethanol adsorption generally desorbs as H_2O or as H_2. H_2O can originate from the recombination of M−H and OH adsorbed from the environment. This product then desorbs, leaving an oxygen vacancy and a partially reduced metal, which, in the presence of gaseous O_2, is reoxidized. Following the reaction of ethoxide formation, dehydrogenation to acetaldehyde results in electron transfer to the metallic site; i.e., ethanol exhibits a reducing behavior.

Figure 8 illustrates the variation of the current flowing through the tin oxide nanobelts as 250 ppm ethanol is introduced in the test chamber at a working temperature of 500 °C and 30% RH.

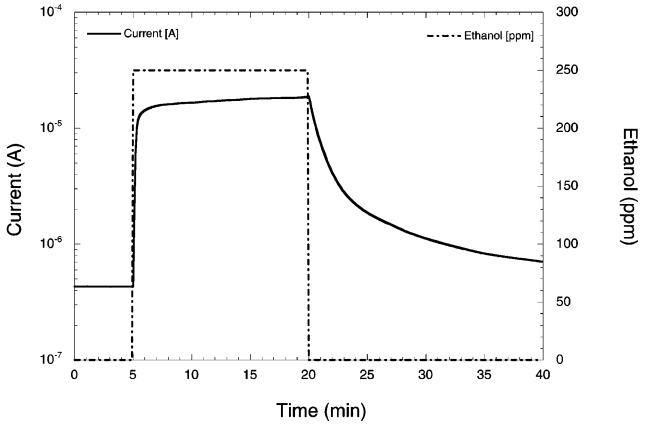

Figure 8. Variation of current flowing through the nanobelts at a working temperature of 500 °C and 30% RH, as 250 ppm ethanol is introduced in the test chamber. The response toward ethanol is very high ($S > 40$), and the response and recovery times are 280 and 90 s, respectively.

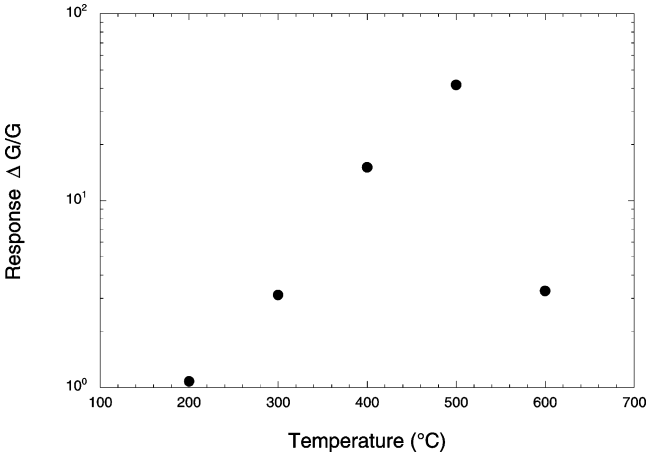

Figure 9. Response of tin oxide nanobelts to 250 ppm ethanol as a function of operating temperature at 30% RH. The response is maximum at 500 °C; this temperature is not correlated with the ionosorbed oxygen coverage since the working principle is not related to oxygen on the semiconductor surface.

The response toward ethanol is very high ($S > 40$), and the response and recovery times are 280 and 90 s, respectively. The response of tin oxide nanobelts is higher with respect to the one found in the literature for tin oxide (300 nm thick, grain size about 20 nm), i.e., 29 toward 500 ppm ethanol at 400 °C.[35]

Figure 9 illustrates the response to ethanol versus operating temperature, which attains a maximum at 500 °C; this temperature is not correlated with the ionosorbed oxygen coverage since, as we have stated previously, the working principle is not related to oxygen on the semiconductor surface.

Finally, the films studied in this work were used for implementation of gas-sensing devices with superior long-term performance due to their peculiarities as reported in refs 7 and 36.

6. Conclusions

We proposed the use of two-dimensional nanostructures of SnO_2 in the form of nanobelts for gas sensing and showed their capability in the determination of NO_2 and ethanol. This topology experimentally showed good electrical responses to gases, comparable to the 3D counterpart. A theoretical explanation for such evidences was inferred: the crucial parameter determining the sensing mechanism, i.e., the depletion layer depth, is not strongly affected by the dimensionality chosen for the system, in the considered range of dimensions. At lower sizes, the model foresees a change in the sensing properties depending on the dimensionality. Structural characterization resulted in a good crystallinity of the films, a feature that guarantees long-term stability with respect to the traditional polycrystalline 3D layers. In conclusion, two-dimensional structures appear to be superior to the conventional 3D ones regarding the basic requirements of a chemoresistive material for its usage as a sensor.

References and Notes

(1) Pavesi, L.; Dal Negro, L.; Mazzoleni, C.; Franzo, G.; Priolo, F. *Nature* **2000**, *408*, 440.
(2) Suryanarayana, C.; Koch, C. C. *Hyperfine Interact.* **2000**, *130*, 5.
(3) Barsan, N.; Weimar, U. *J. Electroceram.* **2001**, *7*, 143.
(4) Gleiter, H. *Nanostruct. Mater.* **1995**, *6*, 3.
(5) Bonini, N.; Carotta, M. C.; Guidi, V.; Malagù, C.; Martinelli, G.; Paglialonga, L.; Sacerdoti M. *Sens. Actuators, B* **2000**, *68*, 274.
(6) Comini, E.; Sberveglieri, G.; Ferroni, M.; Guidi, V.; Frigeri, C.; Boscarino, D. *J. Mater. Res.* **2001**, *16*, 1559.
(7) Comini, E.; Faglia, G.; Sberveglieri, G.; Pan, Z.; Wang, Z. L. *Appl. Phys. Lett.* **2002**, *81*, 1968.
(8) Pan, Z. W.; Dai, Z. R.; Wang, Z. L. *Science* **2001**, *291*, 1947.
(9) Sberveglieri, G.; Depero, L. E.; Groppelli S.; Nelli, P. *Sens. Actuators, B* **1995**, *26*−*27*, 89.
(10) Dai, Z. R.; Gole, J. L.; Stout, J. D.; et al. *J. Phys. Chem. B* **2002**, *106*, 1274.
(11) Flores, F. *Surf. Rev. Lett.* **1995**, *2*, 513.
(12) Brillson, L. J. In *Handbook of Semiconductors*; Moss, T. S., Ed.; Elsevier: Amsterdam, 1992.
(13) Yamazoe, N. *Sens. Actuators, B* **1991**, *5*, 7.
(14) Carotta, M. C.; Ferroni, M.; Guidi, V.; Martinelli, G. *Adv. Mater.* **1999**, *11*, 943.
(15) Tung, R. T. *Phys. Rev. Lett.* **2000**, *84*, 6078.
(16) Hasegawa, H.; Sato, T.; Kasai, S. *Appl. Surf. Sci.* **2000**, *166*, 92.
(17) Léonard F.; Tersoff, J. *Phys. Rev. Lett.* **2000**, *84*, 4693.
(18) Shur, M. In *Physics of semiconductor devices*; Prentice Hall: New York, 1990; pp 140−199.
(19) Rhoderic, E. H.; Williams, R. H. In *Metal-Semiconductor Contacts*; Oxford Science: Oxford, 1988.
(20) Martinelli, G.; Carotta, M. C. *Sens. Actuators, B* **1995**, *23*, 157.
(21) Carotta, C.; Dallara, C.; Martinelli, G.; Passari, L. *Sens. Actuators, B* **1991**, *3*, 191.
(22) Spicer, W. E.; Chye, P. W.; Skeath, P. R.; Su, C. Y.; Lindau, I. *J. Vac. Sci. Technol.* **1979**, *16*, 1422.
(23) Rantala, T. T.; Rantala, T. S.; Lantto, V. *Surf. Sci.* **1999**, *420*, 103.
(24) Malagù, C.; Guidi, V.; Stefancich, M.; Carotta, M. C.; Martinelli, G. *J. Appl. Phys.* **2002**, *91*, 808.
(25) Orton J. W.; Powell, M. *Rep. Prog. Phys.* **1980**, *43*, 81.
(26) Idriss, H.; Seebauer, E. G. *J. Mol. Catal. A: Chem.* **2000**, *152*, 201.
(27) Morrison, S. R. *The Chemical Physics of Surfaces*; Plenum Press: New York, 1977; p 69.
(28) Morrison, S. R. *The Chemical Physics of Surfaces*; Plenum Press: NewYork, 1977; Chapter 2, p 25.
(29) Madou, M. J.; Morrison, S. R. *Chemical Sensing with Solid State Devices*; Academic Press: NewYork, 1988; p 67.
(30) Tamaki, J.; Nagaishi, N.; Teraoka, Y.; Miura N.; Yamazoe, Y. *Surf. Sci.* **1989**, *221*, 183.
(31) Solymosi F.; Kiss, J. *J. Catal.* **1976**, *41*, 202.
(32) Ghiotti, G.; Chiorino, A.; Pan, W. X.; Marchese, L. *Sens. Actuators, B* **1992**, *7*, 691.
(33) Comini, E.; Faglia, G.; Sberveglieri, G. *Sens. Actuators, B* **2001**, *78*, 73.
(34) Comini, E.; Faglia, G.; Sberveglieri, G. *Sens. Actuators, B* **2001**, *76*, 270.
(35) Zampiceni, E.; Comini, E.; Faglia, G.; Sberveglieri, G.; Kaciulis, S.; Pandolfi, L.; Viticoli, S. *Sens. Actuators, B* **2003**, *89*, 225.
(36) Sberveglieri, G.; Comini, E.; Guidi, V.; Malagù, C.; Pan, Z.; Wang, Z. L. *Annual Meeting Abstract of 105th Annual Meeting & Exposition, the American Ceramic Society*; 2003; p 66.